A year of microseisms in southern California

Peter Gerstoft[1] and Toshiro Tanimoto[2]

Received 22 June 2007; revised 29 August 2007; accepted 30 August 2007; published 17 October 2007.

[1] Microseisms are due to continuous harmonic forcing by ocean waves, whose sources vary in time, frequency, and azimuth. Using frequency-domain array beamforming, this variation is studied using one-year of continuous seismic data from 155 stations in southern California. Detailed analysis of data delineates spatiotemporal variations of sources for the primary and secondary microseisms. Both types of microseisms are generated near the coasts but the locations of excitation are different and change with season. Often sources are multiply located but can be spread out over wider areas, especially in the case of secondary microseisms. Distant storms can also be seen occasionally in the frequency range between the primary and secondary microseisms where spectral amplitudes from nearby sources are low. **Citation:** Gerstoft, P., and T. Tanimoto (2007), A year of microseisms in southern California, *Geophys. Res. Lett.*, *34*, L20304, doi:10.1029/2007GL031091.

1. Introduction

[2] Precise observations of spatiotemporal and frequency variations of microseisms are important to understand their physics. Array beamforming seems to be the most useful tool to analyze these aspects of microseisms and we present our analysis for the array in southern California.

[3] Beamforming of microseismic data using a single array has been performed for the LASA array [*Haubrich and McCamy*, 1969] and other arrays [*Cessaro*, 1994; *Friedrich et al.*, 1998]. This line of work tends to focus on time-domain beamforming techniques, including single 3-component stations [*Schulte-Pelkum et al.*, 2004], cross-correlation combined with back propagation [*Stehly et al.*, 2006; *Shapiro et al.*, 2006], azimuthal variations [*Gerstoft et al.*, 2006b] and seasonal variations [*Stehly et al.*, 2006]. We use a frequency-domain beamforming because microseism energy tends to be incoherent across frequency but is spatially coherent as they propagate as Rayleigh waves. Using all sensors in southern California, we can obtain higher resolution for time, frequency and azimuth than previous studies in order to make new observations for understanding the origin of microseisms.

[4] Microseisms can be split into primary and secondary microseisms. Primary microseisms have the same period as the ocean waves (here 0.05–0.08 Hz), whereas secondary microseisms propagate at half the ocean wave period (0.1–0.16 Hz). We present results for 0.03–0.2 Hz, which includes both types of microseisms. Primary microseisms are generated through shoaling of ocean waves [e.g., *Cessaro*, 1994; *Bromirski*, 2001]. Secondary microseisms have larger spectral amplitudes than primary microseisms and large amplitude is likely due to the non-linear interaction of ocean waves as proposed by *Longuet-Higgins* [1950] and expanded by *Tanimoto* [2007a] and *Webb* [2007]. The new theory explains that secondary microseisms are more likely to be generated in shallow water, as observed by many authors [e.g., *Haubrich and McCamy*, 1969; *Bromirski and Duennebier*, 2002; *Bromirski et al.*, 2005; *Rhie and Romanowicz*, 2006; *Tanimoto*, 2007b].

2. Processing

[5] Using continuous data recorded in the year 2006 on all 155 seismic stations (vertical component with sampling rate 1 per second) in southern California, we formed beams and determined the azimuth and slowness of the waves crossing the array as a function of frequency [*Johnson and Dudgeon*, 1993; *Rost and Thomas*, 2002]. The array (Figure 1c) covers a 400 × 600 km area, with a denser station coverage in the Los Angeles basin. A similar processing was used for detecting Katrina in California [*Gerstoft et al.*, 2006a] and proceeds as follows:

[6] First, in the monthly time series, unwanted events (e.g., earthquakes) are removed by truncating signal amplitude above one standard deviation, calculated for the monthly time series. The data is split into 512-s time series, Fourier transformed and corrected for instrument response. For each frequency, we only keep the phase of the signal. Amplitude information is lost here but this will remove undesirable signals caused by local site amplification effects and local large noise event. This is also consistent with the simple plane wave model used in the processing. However, all frequencies will then have equal power, meaning that the typical microseism spectrum will not be retrieved if the resulting power spectrum is extracted. At each frequency, we have a complex-valued vector $\mathbf{v}(\omega, t_i)$ containing the response from the 155 stations, where t_i refers to the time of the Fourier transform. The cross-spectral density matrix is then formed by ensemble averaging († denotes the transpose complex conjugate)

$$\mathbf{C}(\omega, t) = \frac{1}{N}\sum_{n=1}^{N} \mathbf{v}(\omega, t+t_n)\mathbf{v}^\dagger(\omega, t+t_n) \qquad (1)$$

[7] The ith row and jth column of $\mathbf{C}$ contains the average phase delay between the ith and jth seismometer at frequency ω. In the time domain, this would correspond to the cross correlation between the two seismometers. For this study, we used $N = 10$. This corresponds to an averaging time of 10*512 s or 1.5 hour, agreeing well with the minimum resolution time of weather systems.

[1]Scripps Institution of Oceanography, La Jolla, California, USA.
[2]Department of Earth Science, University of California, Santa Barbara, California, USA.

0094-8276/07/2007GL031091$05.00

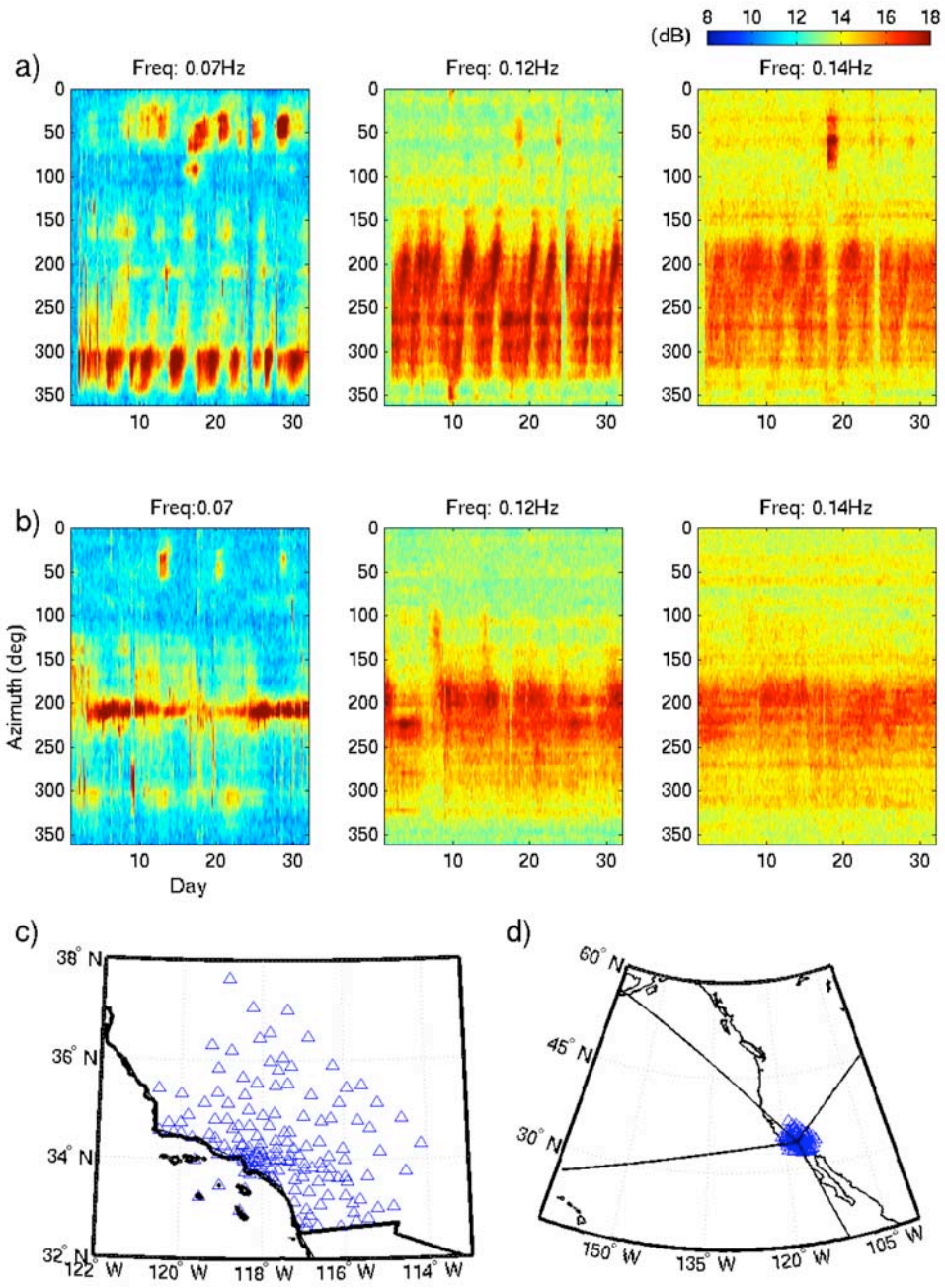

Figure 1. Beamformer output (dB) versus azimuth and days in month for frequencies 0.7, 0.12, and 0.14 Hz during (a) January and (b) July 2006. (c) Station map of the 155 stations. (d) Map of region, showing stations in southern California and important azimuths from the array, 45, 150, 270, 320°.

[8] For a given frequency ω, phase slowness s, and azimuth θ, the plane wave response for the array of geophones is

$$\mathbf{p}(\omega, s, \theta, \mathbf{r}) = \exp\left[i\omega s(\mathbf{r}\,\mathbf{e})\right], \tag{2}$$

where $\mathbf{e} = (\sin\theta, \cos\theta)^{\mathrm{T}}$ is the directional cosines and $\mathbf{r}$ is the coordinates of the geophones with respect to their mean.

[9] The beamforming output is then given by

$$b(\omega, s, \theta, t) = \mathbf{p}^{\dagger}(\omega, s, \theta)\mathbf{C}(\omega, t)\mathbf{p}(\omega, s, \theta) \tag{3}$$

[10] Processing a whole year of data gives a 4-D matrix containing the beamformer output as a function of time, frequency, angle and slowness. There is no averaging across frequency giving a frequency resolution of 1/512 Hz $\approx$ 0.002 Hz. Based on a plane wave simulation, for a 0.1-Hz frequency and phase speed of 3 km/s the array 3-dB beamwidth was 4°. There may be further smearing out of the peaks due to inhomogeneous velocity structure and array bias. A curved wavefront will cause the plane-wave beamformer to degrade, to give high beamformer output for a wider set of angles. This is because the curved wavefront will match the plane waves at several angles. Waves

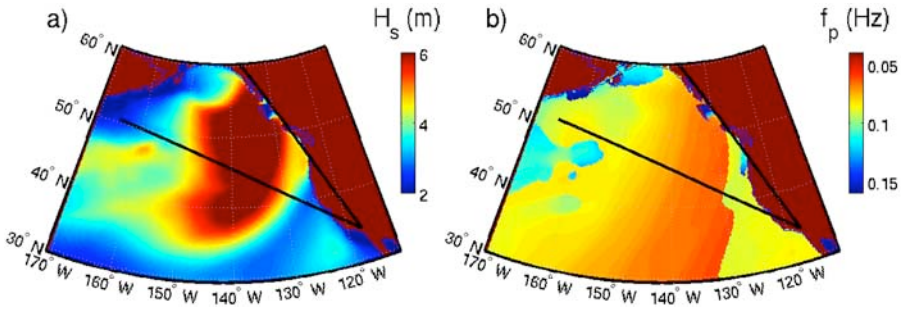

Figure 2. January storm in the North Pacific. In January a string of storms originating from the NW Pacific hit the Pacific coast, here shown for 8 January 21:00 UTC showing (a) significant wave height (m) and (b) peak frequency (Hz). Azimuths 310 and 340° are indicated.

generated close to the array will have a curved wavefront and will thus cause some degradation.

[11] For each frequency analyzed, we searched for the combination of phase slowness and azimuth that gave the best fit to the data. Based on these phase slownesses, it was observed that they are independent of both time and azimuth and showed the Rayleigh wave dispersion with frequency $s = s(\omega)$, similar to the results of *Gerstoft et al.* [2006a]. The dispersion can be determined by averaging over time and azimuth. Thus, the beamformer output only depends on $b(\omega, \theta, t)$.

3. Beamformer Output

[12] The beamformer output is shown in Figure 1 at three frequencies 0.07 Hz (primary microseisms), 0.12 and 0.14 Hz (secondary microseism) for the whole month of January and July, 2006.

[13] In January, a string of storms [*Bancroft*, 2006] hit the Vancouver Island/Oregon area. The seismic noise from most of these storms was detected by the southern California array. An example of such a storm is shown in Figure 2 for 2100 UTC Jan 8, both for the significant wave height and the dominant peak frequency [*Tolman*, 2005]. In the beamformer output (Figures 1a and 1b) the primary microseisms (0.07 Hz) can clearly be seen for azimuths from 310–340°, consistent with a source region in the costal areas of the N Pacific.

[14] After the ocean waves hit the Northern Pacific Coast, ocean waves for the same storm arrives in southern California/Baja California area about a day later (excellent hindcast videos demonstrate this [*Tolman*, 2005]). This can be seen in Figure 1a as striations from about 300° to 160° for all three frequencies. For most of the storms the primary microseisms give a strong response at 160° corresponding to a source region near the coast of Baja California.

[15] Strong microseisms, can be seen from azimuth 40–60° corresponding to a source region in the Northwest Atlantic. The microseisms also correlate well with the storm activity in the Labrador Sea/Northwest Atlantic [*Bancroft*, 2006]. Most of these storms are not easily identifiable in the secondary microseism-bands (Figure 1a), although both primary and secondary microseisms is observed from the storms in the Atlantic (see end of section 4).

[16] For the secondary microseisms (0.12 and 0.14 Hz in Figure 1a), a broad azimuth range from about 160–320° is fairly uniformly activated. This indicates a different source mechanism for the secondary microseisms, as has been advocated by interaction of opposing wave trains. The higher frequencies could be generated more locally, causing a curved wavefront and a less focused beamformer output. A weak response can also be seen at azimuth 140°. This corresponds to microseisms from Gulf of California.

[17] For azimuth 300–340°, both primary and secondary microseisms have been generated in the far field of the array, as their azimuths point to the North California coast. One reason that the primary and the secondary microseisms are weaker in that azimuth is the higher attenuation for high-frequency waves including both scattering and intrinsic attenuation.

[18] In July, the North Pacific is relatively calm and the primary microseisms mainly come from a constant azimuth about 210°. This constant direction does not mean that all storms come from this direction as these waves have been refracted near the coast and propagate perpendicular to the coast. The secondary microseisms are seen from a wider azimuth from 170–270°, again indicating a difference in excitation mechanism.

4. Whole Year

[19] A good overview of the microseisms activity is obtained by examining the azimuth corresponding to the maximum beamformer output. Figure 3 shows variations in azimuth for the whole year in the frequency interval 0.04–0.2 Hz. The main feature is that in the winter months most peak azimuths come from NE (hereafter we use abbreviations for azimuth, N, S, E, and W), whereas in the summer months they come from SSW.

[20] The signature for each storm emerges in Figure 3 as striations, as higher frequencies arrive later. This feature can be explained from the dispersion of the ocean waves [*Haubrich et al.*, 1963] and gives us a clue on distance to the storms. In deep water, the ocean wave group speed at frequency f is given by

$$c_g = \frac{g}{4\pi f} \tag{4}$$

[21] Since propagation of ocean waves in the frequency range 0.04–0.2 Hz can be regarded as those of deep-water waves, if the distance from a storm is R, the arrival time is

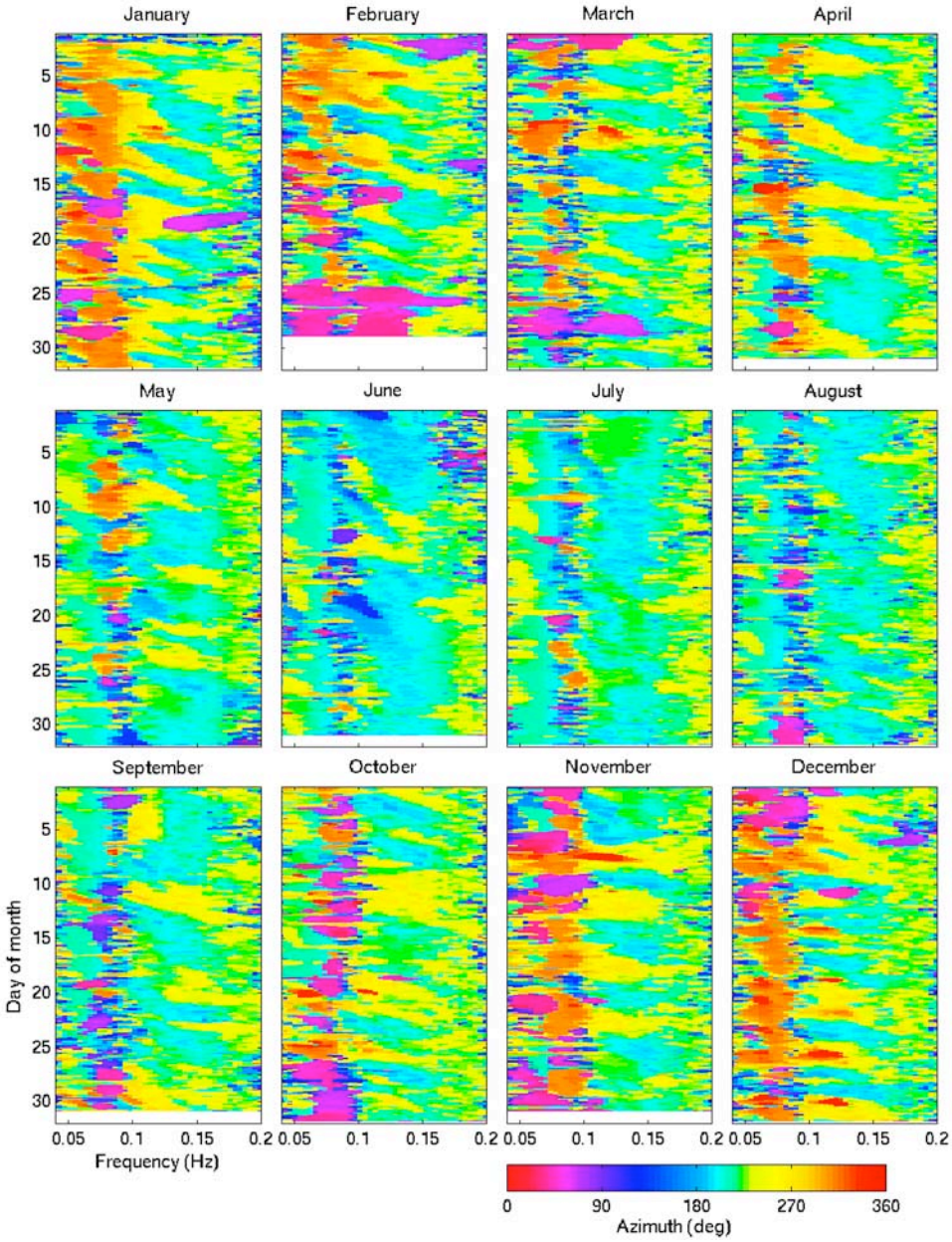

Figure 3. Azimuth (deg) from whole array for each month of 2006. Each panel corresponds to one month.

given as $T = R/c_g = 4\pi f R/g$. From the arrival azimuth versus frequency and time, we can measure the slope $\frac{dT}{df}$ and this gives the distance to the storm

$$R = \frac{dT}{df}\frac{g}{4\pi}. \quad (5)$$

[22] This can be used to determine the distance to the storm if all waves are recorded at the same point. The storms in January (Figure 3) have a slope of 40 days/Hz typically, giving a distance to the storm of 4000 km. This corresponds to the storms originating in the NW Pacific. This can be confirmed by watching the hindcasts [*Tolman*, 2005]. In November and December, the N Pacific storms originate in the NE Pacific and thus the distance to the Pacific coast is considerably less, resulting in a small slope. In the winter (November–February), it is observed that peak azimuth of the primary microseisms comes from NW, but the secondary comes from about W, thus the generation of the microseisms are not at the same point. This will cause a bias in the estimated distances above but the above formula can still be used for a rough estimate.

[23] A few storms in June–September have a steeper slope of 80 days/Hz, giving a distance to the storm of 8000 km. This corresponds to storms in the South Pacific and is in agreement with the hindcasts (see videos [*Tolman*, 2005]) and previous observations [*Haubrich et al.*, 1963].

[24] The fact that we can observe the striations of most storms indicates that the ocean waves have propagated a long distance before coupling into seismic energy. This implies that a major part of the microseisms has been generated along the Pacific Coast.

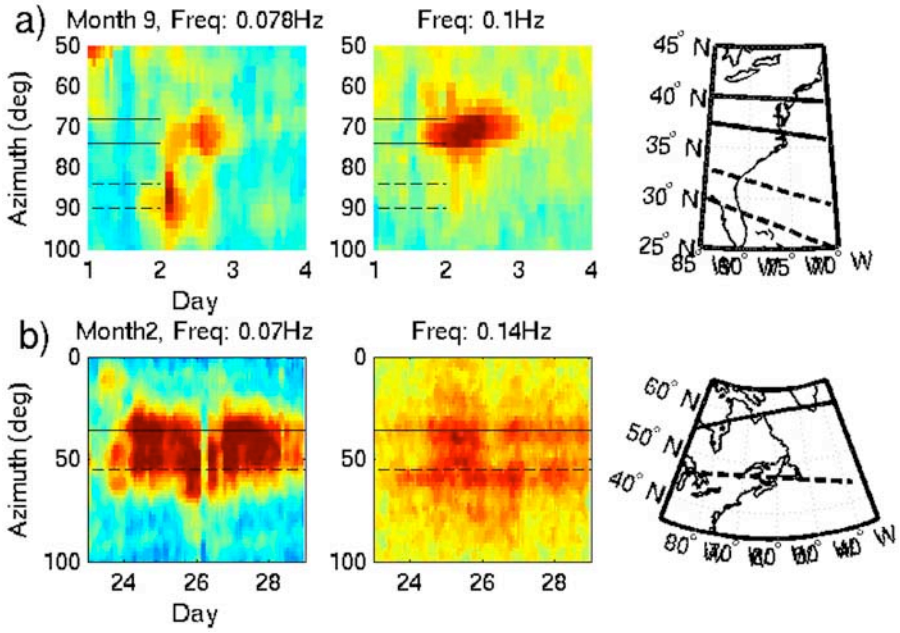

Figure 4. Beamformer output (dB) for two storms in the Atlantic. (a) Tropical storm Ernesto 1–3 September at frequency 0.08 and 0.1 Hz and corresponding map. (b) North Atlantic storm of 24 February to 1 March at frequency 0.7 and 1.4 Hz. The azimuths corresponding to the NE of the Newfoundland/Labrador Peninsula are shown in the map.

[25] The linear signature of the storms can be observed in the primary and especially the secondary microseisms band in Figure 3. This is due to the dispersive nature of the ocean waves and thus a part of the energy in the secondary microseism band is generated by direct interaction with the ocean wave. In general, the secondary microseism is distributed over a large azimuth, 90–180° (Figure 1).

[26] Thus, for both primary and secondary microseisms, the South Pacific storms generate ocean waves that propagate to the coastal areas where they couple into seismic energy. This is confirmed from striations in Figure 3 but also from the very stable 210° azimuth obtained from the beamformer in the primary microseisms band in Figure 1b. This observation is in contrast to *Stehly et al.* [2006] who suggested that the primary microseisms were generated in mid-ocean in the South Pacific and these seismic waves propagated to California. They based their observations on noise cross correlation, for this application it is essentially a 2-point beamforming method.

[27] Spectral low amplitudes are seen between the primary and secondary microseisms (typically, 0.08–0.1 Hz) and it is often possible to observe distant events. In September, signals for tropical storm Ernesto (1–3 Sep), Hurricanes Florence (11–13 Sep) and Helene (25–29 Sep), can be observed. Tropical storm Ernesto was the weakest and made landfall at 4 am UTC 1 September in North Carolina. Microseisms can first be observed a day later from the coast of Georgia (dashed lines in Figure 4a). About 1–1.5 days after landfall, microseisms from the coast of Virginia are observed (solid lines in Figure 4a).

[28] In the summer and fall, noise from NE occurs mostly in the 0.1 Hz spectral low where there is not much power from the Pacific ocean waves. The origin of this noise is not clear as they do not correlate with major storms [*Bancroft*, 2006]. Several storms from The Lawrence Sea can be observed in February and March in primary and secondary microseisms band. According to the Mariners Weather Log (Bancroft, http://www.vos.noaa.gov/mwl.shtml, 2006), Western North Atlantic Storm of February 22 to March 1 developed hurricane force wind. It can be observed with azimuths from 36–50° corresponding to the extent of the Northeast coast of the Labrador Peninsula, see Figure 4. *Schulte-Pelkum et al.* [2004] also observed microseisms in California from the Labrador Sea. Note, that landfast sea ice covers the NE coast of Labrador Peninsula in the winter. Other storms described in the Mariners Weather Log can also be observed: The North Atlantic Storm of February 10–14 and the Western Atlantic storm of March 26–28. Note, that the two Western Atlantic storms generate strongly localized secondary microseisms.

5. Conclusion

[29] Frequency domain beamforming using distributed arrays provides a powerful tool to monitor microseisms.

[30] Microseisms were examined for a whole year with their daily and seasonal variations. From this it is clear that most of the microseisms are generated near the coasts by ocean waves. Based on dispersion of these ocean waves, distance to the storms can be estimated approximately, using the gradient of striation in azimuth vs. frequency plot. In winter, the primary microseisms are dominated by excitation in Northwest direction, thus, North Pacific, but some significant excitation is occurring also in the North Atlantic. Much smaller excitations are also seen off the coast of southern California. In summer, the azimuth of excitation is about 210° suggesting excitation near the coastal area of southern California and mainly excited by ocean waves shoaling in the perpendicular direction to the coast. Excitation of the secondary microseisms occur over wider azimuth

from about 180–320° throughout the year, although the azimuth range is wider in winter. Differences in excitation mechanisms between the primary and secondary microseisms are thus obvious from beamforming results.

[31] Distant storms in the Atlantic can also be seen in the frequency range between the primary and secondary microseisms where spectral amplitudes are generally low from nearby sources. In some cases, even the secondary microseisms generated by these Atlantic storms are seen, although this is relatively rare due probably to (scattering and intrinsic) attenuation effects for these higher frequency waves.

[32] **Acknowledgments.** Funding (to PG) was provided by the US Department of Energy, FA8718-07-C-0005. Data were obtained from the Southern California Earthquake Data Center.

References

Bancroft, G. P. (2006), Marine weather review: North Atlantic area January through April 2006. *Mar. Weather Log.*, *50*(2). (Available at http://www.vos.noaa.gov/mwl.shtml)

Bromirski, P. D. (2001), Vibrations from the "Perfect Storm," *Geochem. Geophys. Geosyst.*, *2*(7), doi:10.1029/2000GC000119.

Bromirski, P. D., and F. K. Duennebier (2002), The near-coastal microseism spectrum: Spatial and temporal wave climate relationships, *J. Geophys. Res.*, *107*(B8), 2166, doi:10.1029/2001JB000265.

Bromirski, P. D., F. K. Duennebier, and R. A. Stephen (2005), Mid-ocean microseisms, *Geochem. Geophys. Geosyst.*, *6*, Q04009, doi:10.1029/2004GC000768.

Cessaro, R. K. (1994), Sources of primary and secondary microseisms, *Bull. Seismol. Soc. Am.*, *84*, 142–148.

Friedrich, A., F. Kruger, and K. Klinge (1998), Ocean-generated microseismic noise located with the Grafenberg array, *J. Seismol.*, *2*, 47–64.

Gerstoft, P., M. C. Fehler, and K. G. Sabra (2006a), When Katrina hit California, *Geophys. Res. Lett.*, *33*, L17308, doi:10.1029/2006GL027270.

Gerstoft, P., K. G. Sabra, P. Roux, W. A. Kuperman, and M. C. Fehler (2006b), Green's functions extraction and surface-wave tomography from microseisms in southern California, *Geophysics*, *71*, S123–S131.

Haubrich, R. A., and K. McCamy (1969), Microseisms: Costal and pelagic sources, *Rev. Geophys.*, *7*(3), 539–571.

Haubrich, R. A., W. H. Munk, and F. E. Snodgrass (1963), Comparative spectra of microseisms and swell, *Bull. Seismol. Soc. Am.*, *53*(1), 27–37.

Johnson, D. H., and D. E. Dudgeon (1993), *Array Signal Processing: Concepts and Techniques*, Prentice-Hall, Upper Saddle River, N. J.

Longuet-Higgins, M. S. (1950), A theory of origin of microseisms, *Philos. Trans. R. Soc. London, Ser. A*, *243*, 1–35.

Rhie, J., and B. Romanowicz (2006), A study of the relation between ocean storms and the Earth's hum, *Geochem. Geophys. Geosyst.*, *7*, Q10004, doi:10.1029/2006GC001274.

Rost, S., and C. Thomas (2002), Array seismology: Methods and applications, *Rev. Geophys.*, *40*(3), 1008, doi:10.1029/2000RG000100.

Schulte-Pelkum, V., P. S. Earle, and F. L. Vernon (2004), Strong directivity of ocean-generated seismic noise, *Geochem. Geophys. Geosyst.*, *5*, Q03004, doi:10.1029/2003GC000520.

Shapiro, N. M., M. H. Ritzwoller, and G. D. Bensen (2006), Source location of the 26 sec microseism from cross-correlations of ambient seismic noise, *Geophys. Res. Lett.*, *33*, L18310, doi:10.1029/2006GL027010.

Stehly, L., M. Campillo, and N. M. Shapiro (2006), A study of the seismic noise from its long-range correlation properties, *J. Geophys. Res.*, *111*, B10306, doi:10.1029/2005JB004237.

Tanimoto, T. (2007a), Excitation of normal modes by nonlinear interaction of ocean waves, *Geophys. J. Int.*, *168*, 571–582, doi:10.1111/j.1365-246X.2006.03240.x.

Tanimoto, T. (2007b), Excitation of microseisms, *Geophys. Res. Lett.*, *34*, L05308, doi:10.1029/2006GL029046.

Tolman, H. L. (2005), User manual and system documentation of WAVEWATCH-III version 2.22, *Tech. Note 222*, NOAA, U.S. Dep. of Comm., Washington, D. C. Hindcast files available from http://polar.ncep.noaa.gov.

Webb, S. C. (2007), The Earth's 'hum' is driven by ocean waves over the continental shelves, *Nature*, *445*, 754–756, doi:10.1038/nature05536.

P. Gerstoft, Scripps Institution of Oceanography, 9500 Gilman Drive, La Jolla, CA 92093-0238, USA. (gerstoft@ucsd.edu)

T. Tanimoto, Department of Earth Science, University of California, Santa Barbara, Webb Hall, Building 526, Santa Barbara, CA 93106, USA. (toshiro@geol.ucsb.edu)